Environmental Science and Pollution Research (2022) 29:58149–58160
https://doi.org/10.1007/s11356-022-19616-x

RESEARCH ARTICLE

A MXene-based multiple catalyst for highly efficient photocatalytic removal of nitrate

Wanying Chen[1] · Bo Wu[2] · Qingzhao Yao[1] · Guomeng Dong[1] · Changjiang Zuo[1] · Yiwei Zhang[1] · Yuming Zhou[1,2] · Yang Liu[3] · Zewu Zhang[1,4]

Received: 2 December 2021 / Accepted: 3 March 2022 / Published online: 1 April 2022

Abstract

Photocatalytic removal of nitrate in wastewater has attracted wide attention because of its simple operation and environmental protection. However, the preparation of photocatalysts with high efficiency and high nitrogen selectivity is still a challenge. In this paper, TiO_2 is grown in situ on Ti_3C_2 MXene by a simple calcination method and modified with silver particles. The presence of Ti_3C_2 reduces the recombination rate of photogenerated electrons and generates more photogenerated electrons. At the same time, the silver particles also increase the photoelectron density and further improve the carrier separation of the catalyst. Due to its unique structure and optical properties, the prepared photocatalyst shows an excellent nitrate removal rate under a high-pressure mercury lamp. At 500 mg_N/L, the nitrate removal rate reaches 96.1%, and the nitrogen selectivity reaches 92.6%. Even after 5 cycles, the prepared photocatalyst still maintains a high nitrate photocatalytic removal efficiency (89%). The electron transfer path is verified by density functional theory calculations.

Keywords TiO_2/MXene · Ag/TiO_2/Ti_3C_2 · Photocatalytic · Nitrate · Nitrite · DFT calculation

Introduction

Excessive nitrate levels in wastewater can lead to the eutrophication of lakes and rivers (Stevens and Gowing 2004; Zhao et al. 2021). Excessive nitrate in drinking water enters the human body and will be converted into nitrite, leading to hypoxia and poisoning of the human body. It can also lead to the blue baby syndrome, methemoglobinemia, and even cancers such as esophageal cancer and gastric cancer (Stevens and Gowing 2004; Zhang et al. 2020a). Therefore, the world health organization recommends that the concentration of nitrate in water should not exceed 11.3mg_N/L (Karen et al. 2010;Loganathan et al. 2013). The concentration of nitrate in drinking water in the USA is set not to exceed 10mg_N/L (Khan and Aspalding 2004). The most commonly used methods for nitrate removal in industry are ion exchange, reverse osmosis, biological method, and bimetallic catalysts. But ion exchange and reverse osmosis only serve to concentrate and transfer nitrate, and the subsequent treatment of the resulting high concentration nitrate wastewater remains a serious challenge (Barrabés and Sá 2011). The removal of nitrate by biological method takes a long time, and the reaction conditions are strict, resulting in biological sludge (Li et al. 2009). Bimetallic catalysts catalyze nitrate to produce nitrogen is a green method, but the reaction requires hydrogen as a reducing agent, hydrogen storage and transportation is a serious challenge for industrial applications (Gao et al. 2019). In recent years, researchers have found that photocatalysis can effectively remove nitrate from wastewater. After studying various semiconductors, such as titanium dioxide (Kim and Pak 2019; Krasae

Responsible Editor: Ricardo A. Torres-Palma

✉ Qingzhao Yao
101006377@seu.edu.cn

[1] School of Chemistry and Chemical Engineering, Southeast University, Jiangsu Optoelectronic Functional Materials and Engineering Laboratory, Nanjing 211189, People's Republic of China

[2] Multiscale Computational Materials Facility, Key Laboratory of Eco-Materials Advanced Technology, College of Materials Science and Engineering, Fuzhou University, Fuzhou 350100, China

[3] Varun Water Environmental Technology Co., Ltd, Taicang 215400, China

[4] School of Materials Science and Engineering, Nanjing Institute of Technology, Nanjing, Jiangsu Province 211167, China

and Wantala 2016; Zhu et al. 2018), cadmium sulfide (Fang et al. 2008; Sittinun Tawkaew et al. 2001), barium tetroxide, and zinc sulfide (Bourkeb and Wbaaloudj 2021), Chu et al. (2013) and Lucchetti et al. (2017) found that titanium dioxide due to its good stability and being non-toxic and a low-cost semiconductor in the photocatalytic removal of nitrate process has a great potential. However, due to its fast complexation of broad-growth charges and relatively wide bandgap, titanium dioxide still suffers from quantum efficiency and low visible light utilization (Hirayama and Kamiya 2014; Xiong et al. 2018). Single photocatalyst has a high photoelectron-hole recombination ratio, which affects the reaction efficiency of photocatalysis. The use of cocatalyst can effectively promote the separation of photogenerated electrons and holes (Zhao et al. 2020).

MXene is a new type of 2D transition metal carbide or carbonitride, which is produced by HF etching the Al-containing layer of MAX ceramics (Sreedhar and Noh 2021). Since it was first reported by Naguib et al. (2011), its graphene-like structure, hydrophilic layered surface, and significant conductivity properties have been widely considered as good candidates for energy storage, electrochemical sensors, and pollutant purification (Zhao et al. 2017). In the field of photocatalysis, MXene has many advantages that make it an efficient cocatalyst for photocatalysts. First, MXene has hydrophilic properties, which facilitate the adsorption of water molecules by photocatalysts, thus promoting the water separation reaction of photocatalysis (Khadidja et al. 2021). Secondly, MXene has a large number of hydrophilic functional groups (such as -OH) on the surface, which can be combined with most semiconductor photocatalysts and have a strong interaction with semiconductor photocatalysts (Hong et al. 2020). The Gibbs free energy of hydrogen adsorption of MXene is close to zero, which is conducive to the reduction of H^+ to H_2, and has a high activation energy of hydrogen precipitation. In addition, Ti_3C_2 MXene highlights specific surface areas and inhibits charge carrier recombination during photocatalytic activity (Naguib et al. 2014). Surprisingly, the carrier separation is enhanced when titanium dioxide is in close contact with Ti_3C_2 (Feng et al. 2021). In conclusion, Ti_3C_2 MXene is very beneficial in photocatalytic applications (Quyen et al. 2021). In addition to the addition of cocatalyst, there are the following methods to improve the separation of photogenerated electron-hole pairs in TiO_2: combining with another semiconductor (Sivakumar et al. 2013) or a point-based material (Wu et al. 2002), such as graphene, doping transition metal ions (Rathinavelu et al. 2013) or noble metal elements (Tian et al. 2015), or depositing metal nanoparticles on semiconductor surface (Zhang et al. 2009). A certain sacrificial agent is added to the reaction (Shi et al. 2011).

Hence, this paper presents a method to grow TiO2 nanoparticles in situ on MXene surface by simple calcination and finds that the loading of TiO2 nanoparticles can be tuned by adjusting the calcination temperature. TiO_2/Ti_3C_2 supported with silver particles was prepared as an efficient photocatalyst for nitrate removal. Under the irradiation of a high-pressure mercury lamp, the removal effect of the catalyst on nitrate was investigated and its mechanism was discussed.

Experimental details

Sample preparation

Materials

Aluminum carbon titanite, hydrofluoric acid, silver nitrate, sodium borohydride, potassium nitrate, sodium potassium dodecylate, formic acid, and sodium hydroxide were purchased from Sinopagic Chemical Reagent Co. LTD, without further treatment. All the water used for reagents was deionized.

Preparation of Ti_3C_2

Ti_3C_2 powder was prepared by the reaction of hydrofluoric acid with Ti_3AlC_2. 1.2 g of Ti_3AlC_2 powder was slowly added into 21 mL, 48% hydrofluoric acid and stirred at room temperature with a magnetic stirrer at 500 r/min for 36 h to etch the aluminum layer, and finally an accordion-like solid powder was obtained. The black precipitate obtained was centrifuged and washed with deionized water until its supernatant was neutral. The obtained solid was dried in an oven at 80°C for 12 h to obtain Ti_3C_2 powder (Huang et al. 2020).

Preparation of TiO_2/Ti_3C_2 composite

TiO_2/Ti_3C_2 composite was prepared by simple calcination. 0.5g dried and ground Ti_3C_2 was weighed and put into a tubular furnace at a heating rate of 10°C/min. TiO_2/Ti_3C_2 composite was obtained by calcination at 250 °C, 350 °C, 450 °C, 550 °C, and 650 °C respectively for 1h, which was recorded as $tTTiO_2$, which t stands for calcination temperatures, such as 250 °C, 350 °C, 450 °C, 550 °C, or 650 °C.

Preparation of $Ag/TiO_2/Ti_3C_2$

$Ag/TiO_2/Ti_3C_2$ catalyst was prepared by simple chemical reduction method (Zhang et al. 2003). 0.5g TiO_2/Ti_3C_2 powder was weighed and put into 10mL water. $AgNO_3$ (0.008g, 0.016g, 0.024g, 0.032g, 0.04g) was added to the solution as Ag source, and then 0.005g sodium dodecyl sulfate was added as dispersant, and stirred for 30 min. Then, 0.05g solid sodium borohydride was dissolved in 10mL 1M NaOH solution, and the solution was added drop by drop into $TiO_2/$

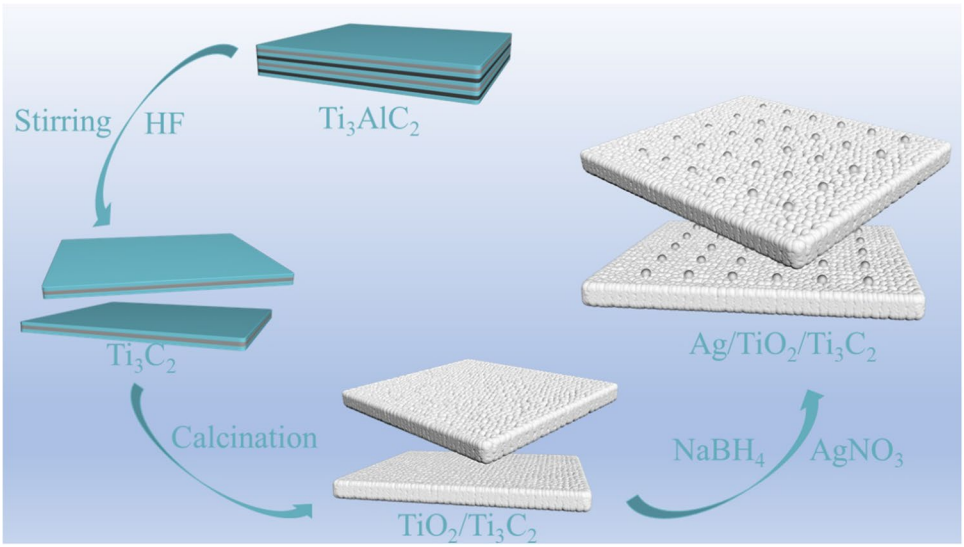

Scheme 1 The synthesis process of TTA

Ti_3C_2 solution, stirred for 30 min, centrifuged, cleaned with deionized water, and dried to obtain $Ag/TiO_2/Ti_3C_2$ solid, denoted as nTTA, which n represents the mass fraction of loaded silver, such as 1%, 2%, 3%, 4%, or 5%.

The synthesis process of TTA is shown in Scheme 1.

Characterization

The crystal structure of the samples was characterized by X-ray diffraction (XRD) (Ultima IV, Japan). Scanning electron microscopy (JEOL JSM-5600L SEM) and transmission electron microscope (TEM, JEM-2010) were used to observe the morphology, microstructure, and elemental analysis of the samples. BET analysis of the samples was performed using Micromeritics (ASAP 2020). The pore size distribution of mesoporous materials was analyzed by using Barrett-Joyner-Halenda (BJH) model. $BaSO_4$ was used as the background to test the UV-visible diffuse reflectance spectrum (UV-VIS DRS) of the sample using Shimadzu ULTRAVIOLET visible spectrophotometer (UV 3600, Shimadzu). The surface chemical composition was analyzed by X-ray photoelectron spectroscopy (XPS) using Mg Kα radiation.

Photoelectrochemical measurements

Use 200mL, 0.1M Na_2SO_4 solution as an electrolyte solution, use the standard three-electrode system, use sample as working electrode, platinum as counter electrode, and Ag/AgCl (saturated KCl) as a reference electrode. Before the start of the test, 2 mg of the sample was added to 0.5 mL of water, 0.5 mL of ethanol, and 20 µL of Nafion, and dispersed by ultrasound. The suspension was smeared on FTO glass with a fixed area of 0.5 cm^2. Finally, the FTO glass coated with the suspension was placed in an oven at 160 °C overnight to obtain a working electrode.

Photocatalytic denitrification performance

The photocatalytic reduction of nitrate was carried out in a 250mL borosilicate reactor. The light source is a 250W high-pressure mercury lamp (the main wavelength is about 365 nm). The initial nitrate concentration is 500 mg_N/L (by weight of nitrogen). There is no treatment of dissolved oxygen. Twenty milligrams of the catalyst was added to 50 mL water, and the solution was stirred in the dark for 30 min to achieve the adsorption-desorption equilibrium of nitrate nitrogen. Then, 40 mM formic acid solution was added as a cavity cleaner (Soares et al. 2014). Turn on the condensate so that the reaction always takes place at room temperature during the photocatalytic process. In the photocatalytic reaction process, the liquid is extracted from the reactor regularly, the concentration of nitrate is detected by using the lightning ion concentration detector (PXS-270), the nitrite and ammonium are detected by using a spectrophotometer (UV722), and the total nitrogen is tested by using an ultraviolet spectrophotometer (UV-3600). Since nitrite, ammonia, and nitrogen are the main products in the photocatalytic process, NO and N_2O by-products can be ignored, and organic nitrogen will not be generated. Therefore, the selectivity of N_2 is calculated according to the following formula:

$$S(N_2) = \left[C(NO_3^-)_0 - C(NO_2^-)_t - C(NH_4^+)_t - C(NO_3^-)_t\right] / \left[C(NO_3^-)_0 - C(NO_3^-)_t\right] \quad (1)$$

where $S(N_2)$ represents the selectivity of N_2, $C(NO_3^-)_0$ represents the initial concentration of nitrate nitrogen content, and $C(NO_3^-)_t$, $C(NO_2^-)_t$, and $C(NH_4^+)_t$ represents the nitrogen content of each ion after t time reaction.

DFT calculation method

In this work, the density functional theory (DFT) calculation was performed by the Vienna Ab-initio Simulation Package (VASP) code, in which a plane wave basis set was used (Meng et al. 2017). The exchange and correlation interactions were modeled using the generalized gradient approximation (GGA) and the Perdew-Burke-Ernzerhof (PBE) functional (Zhang et al. 2020b). Grimme's semi-empirical DFT was introduced in the computations to guarantee a better description of the electron interaction in a long range. The Vanderbilt ultrasoft pseudopotential was used with a cutoff energy of 450 eV (Bredas and Lhouk 2014). Geometric convergence tolerances were set for a maximum force of 0.02 eV/A° and a maximum energy change of 10^{-5} eV/ato. Density mixing electronic minimization was implemented and the self-consistent field (SCF) tolerance was set to the high accuracy of 10-5 eV/atom for energy convergence.

Result and discussion

The morphology and element distribution of the samples were analyzed by scanning electron microscope (SEM) and energy-dispersive X-ray spectrometer (EDS) (Mao et al. 2021). As shown in Fig. 1a and b, the etched Ti_3C_2 has a hierarchical accordion-like structure and is smooth. The surface of TiO_2/Ti_3C_2 after calcination becomes rough, which is due to the formation of TiO_2 nanoparticles on the surface (Fig. 1c). In addition, with the increase of the calcination temperature, the color of TiO_2/Ti_3C_2 became whiter and whiter (Fig. S1), and the TiO_2 particles formed on the surface became more and more dense, like a crispy pot (Fig. 1d, Fig. S2a–d). In this paper, $TTiO_2$ calcined at 550°C was used for the subsequent study of supporting Ag. After loading Ag, the morphology of the sample did not change significantly (Fig. 1e). The sample was tested by

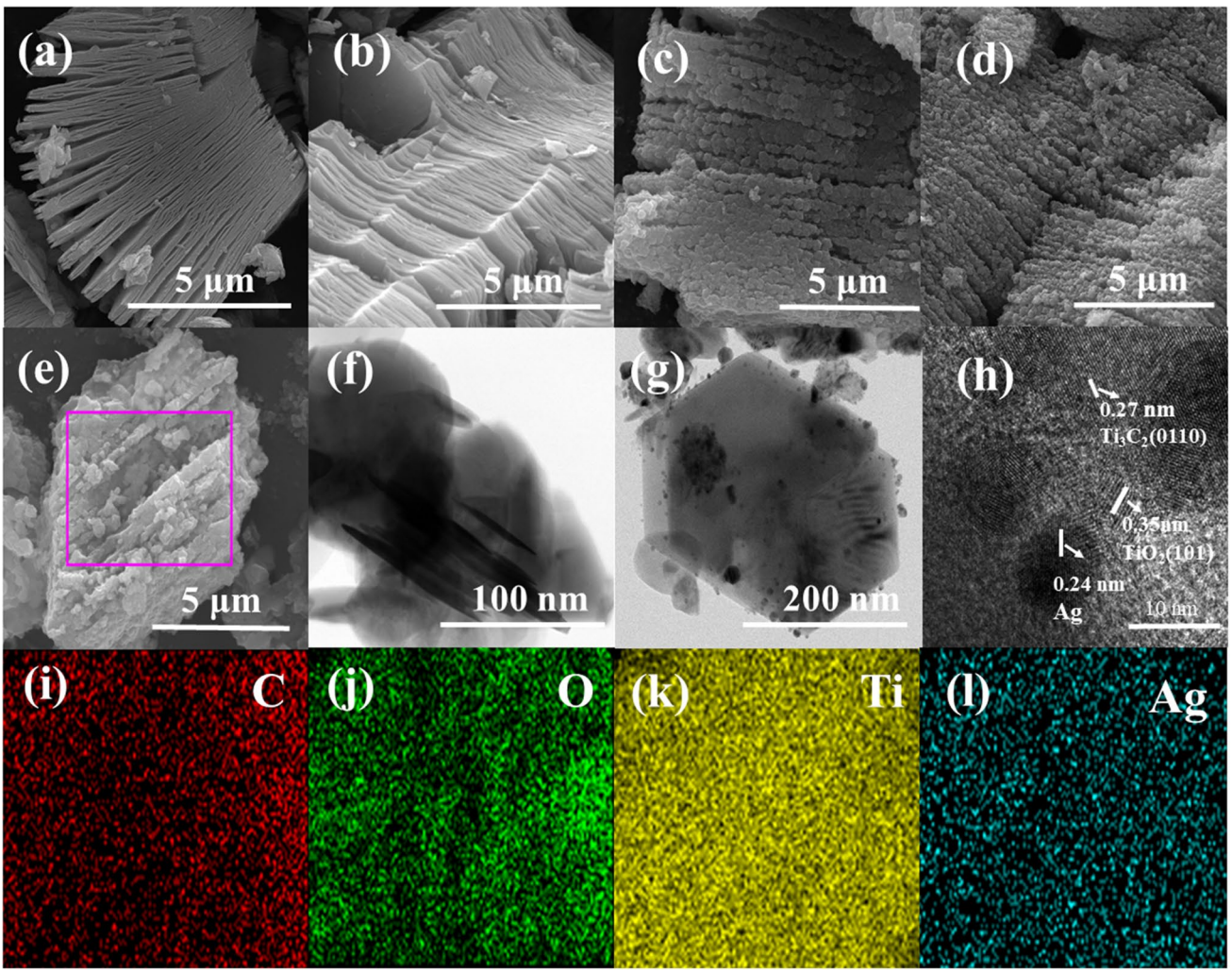

Fig. 1 SEM images of **a**–**b** Ti_3C_2, **c** $350TTiO_2$, **d** $550TTiO_2$, **e** 3%TTA, HRTEM images of **f** Ti_3C_2, **e**–**h** 3%TTA, **i**–**l** elemental mappings of **e**

TEM. Figure 1f shows the clear layered structure of Ti_3C_2, which also indicates that the transformation of Ti_3C_2 into TiO_2 starts from the surface of Ti_3C_2 and extends to the core of Ti_3C_2. Taking 3%TTA as an example, After Ag was loaded, Ag particles were attached to the surface of 550TTiO_2 (Fig. 1g). It can be seen that TiO_2 is located on the surface of Ti_3C_2, and Ag particles are supported on the surface of TiO_2. The lattice and fringe spacing were determined by high-resolution transmission electron microscopy (TEM). The lattice fringes of Ag, TiO_2, and Ti_3C_2 are visible, indicating the successful preparation of TTA (Fig. 1h) (He et al. 2021). Among them, the lattice spacing of 0.24 nm, 0.35 nm, and 0.27 nm is attributed to the (101) face of Ag, the (101) planes of anatase TiO_2, and the (0110) planes of Ti_3C_2, respectively. In addition, the elemental analysis spectrum of TTA was measured. It can be seen from Fig. 1i–l that Ag is uniformly distributed on 550TTiO_2.

The X-ray diffractograms of all samples are shown in Fig. 2. After HF acid etching, the diffraction line located at 39° of (104) plane disappeared in Ti_3C_2 compared with Ti_3AlC_2, indicating that HF acid etched off the Al layer and Ti_3AlC_2 transformed into Ti_3C_2 (Yu et al. 2019). After HF etching, the Ti_3C_2 layer spacing increased and the 004 plane underwent a smaller angle shift, which also proved the successful etching of Ti_3C_2 (Li 2019). After calcination at 250 °C, the cleanliness of Ti_3C_2 increased and the diffraction lines were enhanced. In addition, the appearance of TiO_2 anatase diffraction lines was also observed, indicating the generation of TiO_2. With the increase of the calcination temperature, the content of TiO_2 also increased, the crystallinity of TiO_2 increased, the defect of the sample decreased, and the intensity of the TiO_2 diffraction line gradually increased. Shrinkage of surface defects reduces the possibility of electron-hole recombination (Fig. 2a). In addition, Ti_3C_2 diffraction lines appeared at 35° and 43° in the samples calcined at 250 to 650 °C, confirming the formation of TiO_2/Ti_3C_2 composite materials. Moreover, with the increase of calcination temperature, the intensity of the Ti_3C_2 diffraction line gradually decreases, which proves that Ti_3C_2 transforms into TiO_2. At 650 °C, the peak of Ti_3C_2 completely disappeared, proving that Ti_3C_2 was completely converted to TiO_2 (Fig. 2b) (Hou et al. 2021). It is proved that the yield of TiO_2 can be easily adjusted by changing the calcination temperature. With the increase of Ag loading, Ag peaks gradually appeared at 44°, 64°, and 78° (Fig. 2c and d) (Jia et al. 2016).

Due to the calcination of Ti_3C_2, the surface composition of Ti_3C_2 changes. To further confirm the changes of surface composition and chemical states of the samples, XPS characterization was carried out. The samples were Ti_3C_2, 550TTiO_2, 650TTiO_2, and 3%TTA. Obviously, the binding energy peaks of the Ti element were observed in all four samples (Fig. 3a). Eight peaks can be seen in the high-resolution Ti 2p, as shown in Fig. 3b. 454.9 eV, 460.8 eV, 455.9 eV, 461.5 eV, 457.5 eV, 463.5 eV, 459 eV, and 465.7 eV, respectively, correspond to the Ti - C $2p_{3/2}$, Ti - C $2p_{1/2}$, Ti^{2+} $2p_{3/2}$, Ti^{2+} $2p_{1/2}$, Ti^{3+} $2p_{1/2}$, Ti^{3+} $2p_{1/2}$, TiO_2 $2p_{3/2}$, and TiO_2

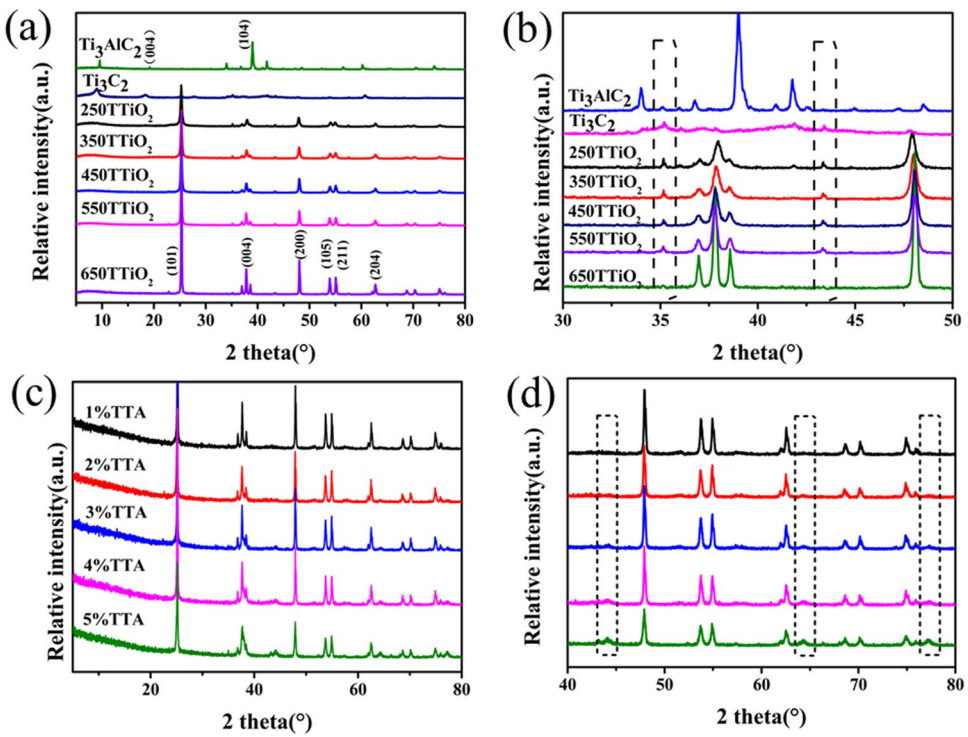

Fig. 2 **a** X-ray diffraction (XRD) of TTiO_2; **b** magnified XRD patterns of **a**; **c** X-ray diffraction (XRD) of TTA; **d** magnified XRD patterns of **c**

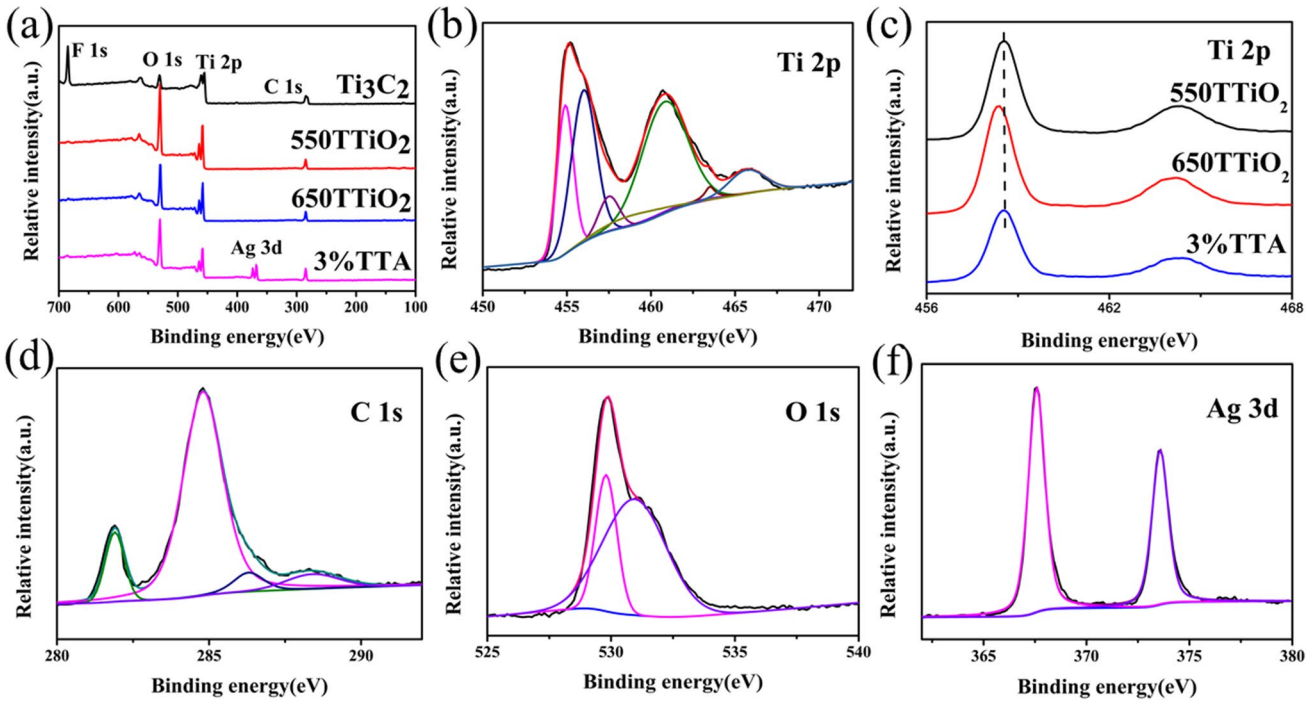

Fig. 3 **a** X-ray photoelectron spectroscopy (XPS) survey spectra of Ti_3C_2 and 550TTiO_2. High-resolution Ti 2p XPS spectra of **b** Ti_3C_2 and **c** 550TTiO_2 and 650TTiO_2. High-resolution C 1s (**a**), O 1s (**b**), and Ag 3d (**c**) XPS spectra of 3%TTA

$2p_{1/2}$. Consistent with previous reports (Shah et al. 2016). Compared with Ti calcined at 550 °C and 650 °C for 1h, only the main binding energy peaks of TiO_2 $2p_{3/2}$ and TiO_2 $2p_{1/2}$ at 459 eV and 464.4 eV were observed in the calcined samples, but there was no binding energy peak of Ti_3C_2 (Fig. 3c), which was not consistent with the XRD description. This is because XPS can only detect the components of the surface layer of the sample, that is, the components with a depth of less than 5nm, making it difficult for XPS to detect Ti_3C_2 located in the interior. As shown in Fig. S3 a, the XPS spectra of C1s of Ti_3C_2 have peaks at 281.9 eV, 284.7 eV, 286.4 eV, and 288.7 eV, corresponding to C-Ti-T_{xa}, C-C, CO-, and COO-, respectively (Halim et al. 2016). These are attributed to Ti_3C_2 and amorphous carbon. In the sample calcined at 550 °C for 1h, its C spectrum has four peaks. Compared with the peak of Ti_3C_2, the peak at 281.9 eV of the sample calcined at 550 °C decreases in intensity, indicating that a part of Ti_3C_2 is converted into TiO_2, while the sample calcined at 650 °C does not have the peak of C-Ti-O_x at 281.9 eV (Ghassemi et al. 2014). It is proved that Ti_3C_2 is completely converted to TiO_2, which is consistent with XRD results (Fig. S3b–c). For the XPS peak of O1s, with the increase of calcination temperature, the peak intensity of C-Ti-$(OH)_x$ and C-Ti-O_x decreases, while the peak intensity of Ti-O increases, proving that Ti_3C_2 transforms to TiO_2 (Fig. S3d–f). For Ag-loaded samples (Fig. 3d–f), silver XPS showed two peaks at 367.58 eV and 373.58eV, corresponding to Ag $3d_{5/2}$ and Ag $3d_{3/2}$, respectively. The bimodal separation values of Ag $3d_{5/2}$ and Ag $3d_{3/2}$ are 6 eV, which is consistent with the most common values reported in the literature (Nila et al. 2019).

The optical bandgap energy (Eg) for the sample can be obtained by UV-vis spectra, corresponding to the intercept of the $(\alpha h\nu)^{1/2}$ curve. As shown in Fig. 4b, Eg values of 1%TTA, 2%TTA, 3%TTA, 4%TTA, and 5%TTA were 3.18 eV, 3 eV,3.2 eV, 3.17 eV, and 3.16 eV, respectively. The detailed band structure of the sample can be obtained by testing the Motshott curve and shown in Fig. 4c. The X-intercept of the Mott-Schottky diagram represents the conduction potential $E_{(CB)}$ of the prepared N-type semiconductor (Baldini et al. 2020). The $E_{(fb)}$ value is estimated from the line segment of the X-intercept of the Mott-Schottky diagram. According to different reference electrodes, the conduction potential $E_{(CB)}$ can be calculated by $E_{(fb)}$. The results are shown in Table S1. Therefore, in combination with the bandgap energy measured by UV-VIS spectroscopy, valence band potential $E_{(VB)}$ can be obtained by formula (2) :

$$E_{(VB)} = Eg + E_{(CB)} \quad (2)$$

As shown in Fig. 4d, the arrangement diagram of the energy band structure of TTA was obtained through calculation (Fernández-Domene et al. 2016).

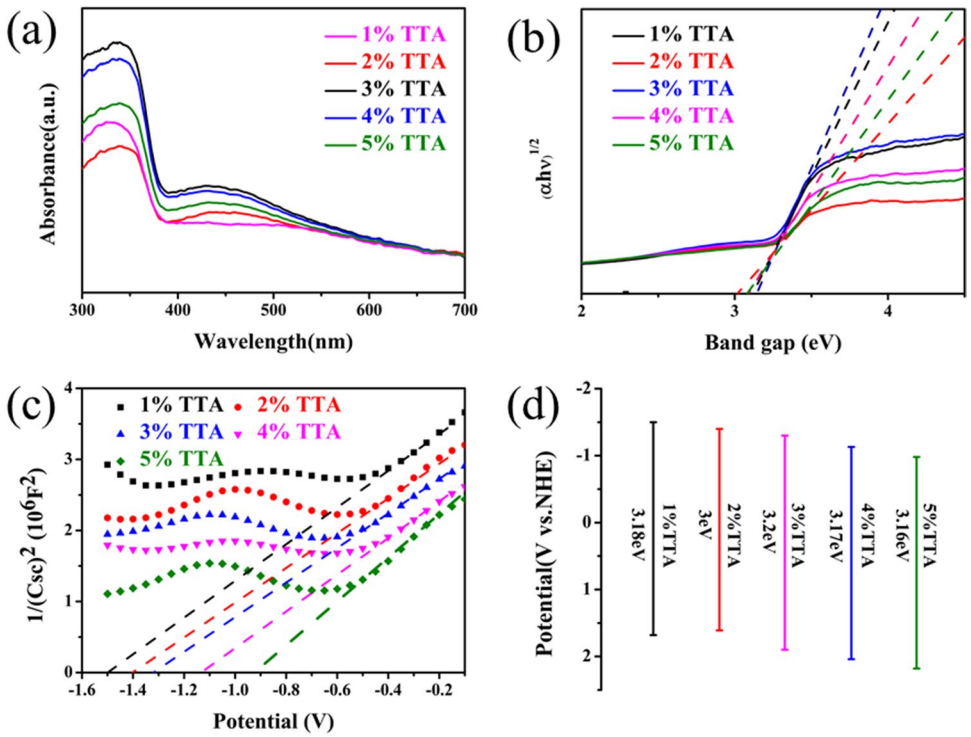

Fig. 4 **a** UV-Vis DRS spectra; **b** bandgap obtained by Tauc schemes of the samples; **c** Mott-Schottky curves; **d** the flat-band potential $E_{(fb)}$ estimated by Mott-Schottky curves

To study the separation and transfer of photogenerated electrons, EIS tests were performed on the samples (Zhang et al. 2020c). As shown in Fig. 5a, the impedance arc radius of the Nyquist plots (TTA) decreased with the increase of Ag content, indicating that the Ag loading can reduce the resistance of charge transfer and enhance charge separation in the system. To further confirm carrier separation, transient photocurrent response tests were performed (Fig. 5b). The photoresponse of photocatalyst shows transient stable photocurrent when the lamp is turned on, and returns to dark current state quickly when the lamp is turned off. The photocurrent density of TTA increased first and then decreased with the

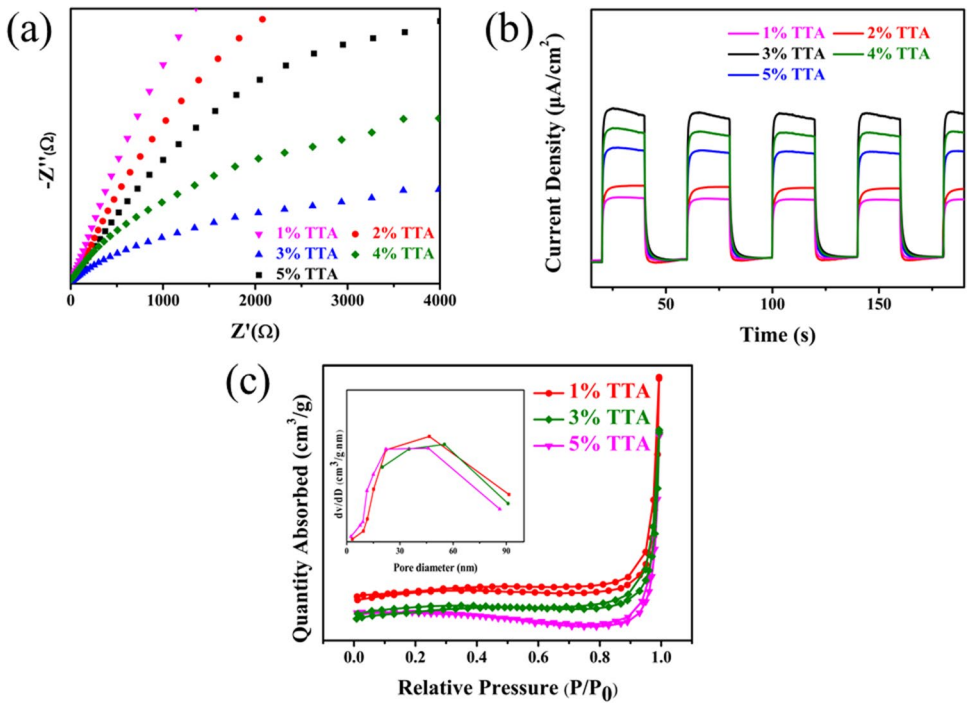

Fig. 5 **a** EIS Nyquist plots; **b** transient photocurrent response curves; **c** nitrogen adsorption-desorption isotherms of the samples work

increase of silver content, and reached the maximum value at 3%TTA. Through the analysis of electrochemical impedance and photogenerated current spectrum, it is concluded that silver particles and Ti_3C_2 can effectively capture and conduct photogenerated electrons and inhibit the recombination of charge carriers. N_2 isotherm adsorption-desorption curve is shown in Fig. 5c and Fig. S4. For $TTiO_2$, as the calcination temperature increases, the specific surface area of the sample increases, proving that more and more TiO_2 are generated. As silver loading increases, specific surface area decreases. According to Brunauer-Deming-Deming-Teller (BDDT) classification, the adsorption isotherms of the samples were class iv isotherms, indicating the presence of mesopores (2–50nm) (Low et al. 2014).

To verify the electron transfer path of samples, density functional theory (DFT) calculation was carried out for some samples, such as Fig. S5 (TiO_2 (101), Ti_3C_2(001)) (Chen et al. 2020; Meng et al. 2018). Obviously, the alternating arrangement of Ti and C atomic layers forms the layered structure of Ti_3C_2, and the calculated bandgap is TiO_2 (3.17 eV) and $TTiO_2$ (−0.0305 eV). It can be speculated that band overlap leads to the disappearance of the bandgap. The total and partial state densities of Ti_3C_2, TiO_2, and Ag are shown in Figure 6. In order to further explain the electron transfer path, the Fermi energy levels of Ag, TiO_2, and Ti_3C_2 are calculated by DFT, which are 1.662eV, 9.149eV, and 3.542eV, respectively. The electrons should tend to transfer from the material with a high Fermi energy level to the material with a low Fermi energy level, that is, the electrons should transfer from TiO_2 to Ag and Ti_3C_2.

$TTiO_2$ calcined at 550 °C was used as the carrier and supported with different contents of Ag to carry out photocatalytic reactions of nitrate. The photocatalytic reduction capacity of the catalysts with different Ag contents for nitrate

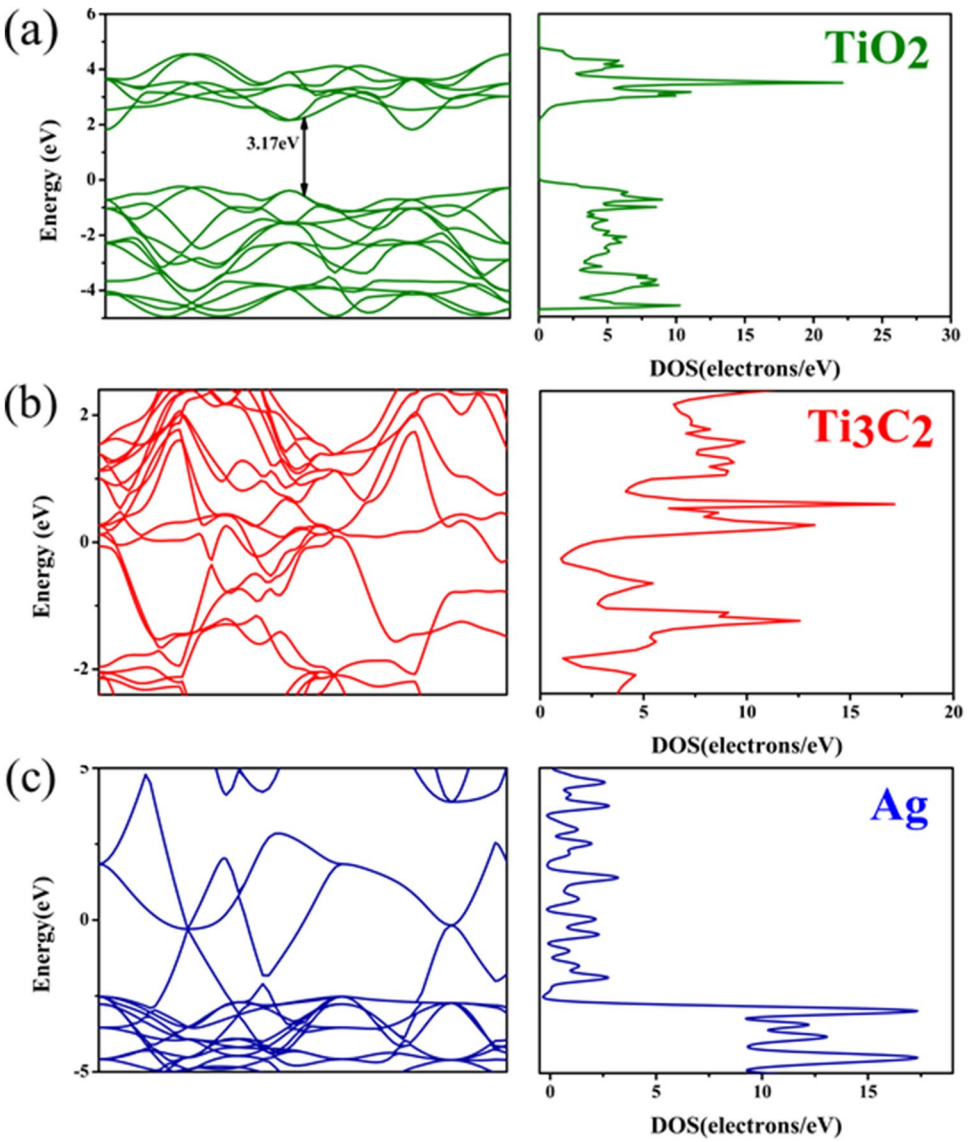

Fig. 6 The band structures and DOS for **a** TiO_2, **b** Ti_3C_2, **c** Ag

was 3%TTA > 4%TTA > 5%TTA > 2%TTA > 1%TTA. When the Ag loading does not exceed 3%, it can be seen that with the increase of Ag loading, the nitrate removal rate also increases. But, when the silver loading exceeds 3%, the nitrate removal rate decreases rapidly with the increase of silver loading. The reason may be that there is too much silver on the surface of TiO_2, so that the silver particles agglomerate, thus reducing the number of active sites. After 4 h of reaction time, 3% TTA showed the highest nitrate removal rate (96.1%) (Fig. 7a). At the same time, kinetic curve fitting was carried out (Mao and X-p 2017). As shown in Fig. 7b, it was found that the reaction conforms to the reaction kinetic model ($-\ln(C/C_0)= Kt$), where C_0 represents the initial concentration of nitrate, C represents the concentration of nitrate after t reaction time, and K represents the reaction rate constant. 3%TTA shows the highest photocatalytic dynamic performance. The kinetic rate constant is the highest, which is three times that of 1%TTA, as shown in Fig. S2. Subsequently, 3%TTA was used for further study. The photocatalytic removal of nitrate (500mg/L) with 3%TTA was studied, and the nitrate removal rate reached 96.1% and nitrogen selectivity reached 92.6% within 4h (Fig. 7c). Nitrate is first reduced to N_2, NO_2^-, and NH_4^+ in the photocatalytic removal process (Challagulla et al. 2017). Nitrite, acting as an intermediate, accumulates in the initial stage and is subsequently converted to NH_4^+ and N_2. Although some NO_3^- and NO_2^- are overreduced to form NH_4^+, the residual concentration of NH_4^+ is very low. Cyclic experiments showed that 3%TTA had strong stability, and the nitrate removal rate was still 89% after 5 rounds of experiments (Fig. 7d).

The photocatalytic mechanism of TTA is shown in Scheme.2. Under light irradiation, electrons on the valence band (VB) of TiO_2 nanocrystals are excited to the conduction band (CB), generating photogenerated electrons and holes (Fuxiang Zhang et al. 2004a) (Eq. (2)). The photogenerated

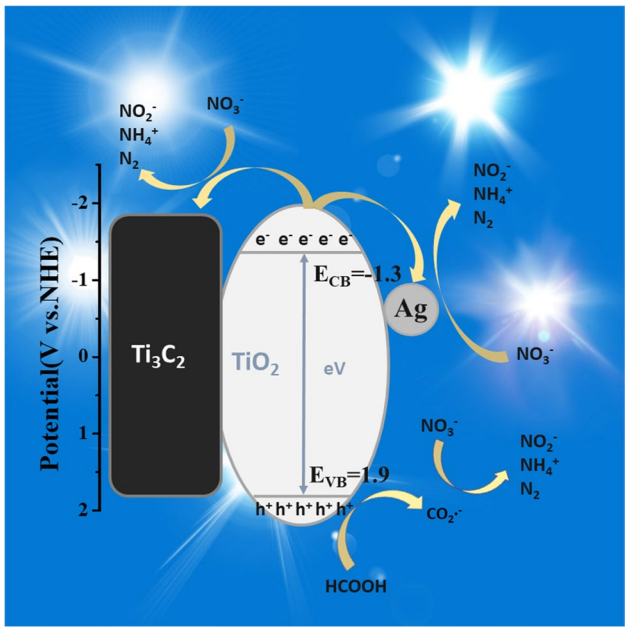

Scheme 2 The photocatalytic mechanism of TTA

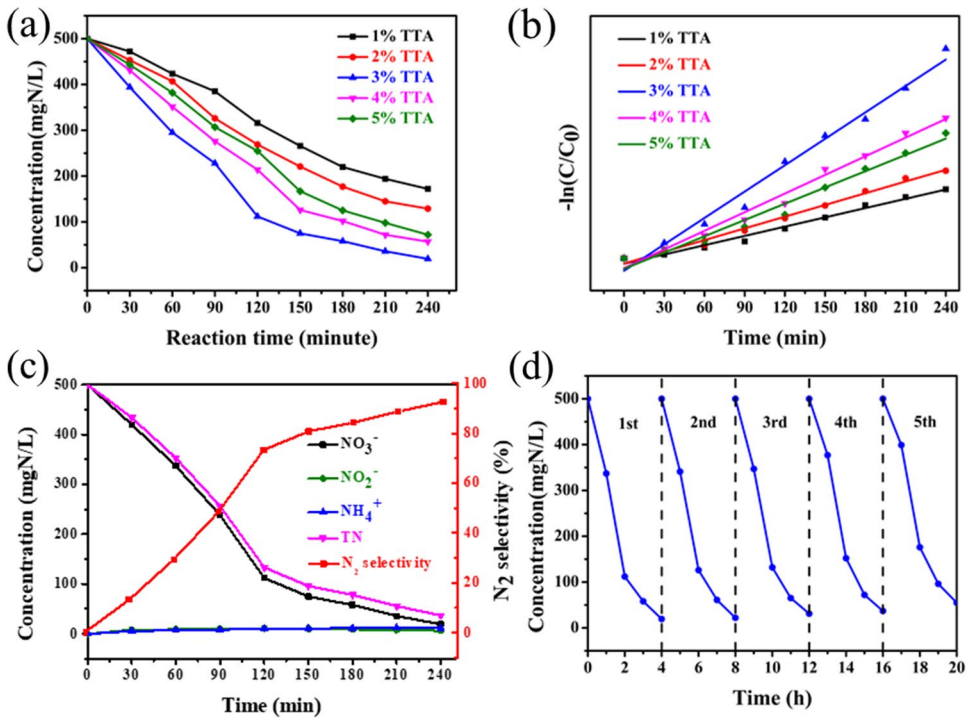

Fig. 7 **a** Photocatalytic reduction of low concentration nitrate (C_0 =500 mg_N/L) over different photocatalysts, **b** kinetic curves fit by first-order kinetic equation, **c** NO_3^-, NO_2^-, NH_4^+, and N_2 selectivity during the process of photocatalytic denitrification (C_0 =500 mg_N/L), **d** the cycling experiment of 3% TTA for photocatalytic reduction of nitrate (C_0 =500 mg_N/L)

electrons further migrate to Ti_3C_2. This process allows charge separation, protects the charge carriers from rapid compounding, and maximizes the electron lifetime (Zhang et al. 2004b). The electron absorption effect of Ag nanoparticles promotes the transfer of photogenerated electrons from the conduction band (CB) of TiO_2 to Ag nanoparticles, facilitating the electron-hole separation. The electrons generated by TiO_2 can react directly with NO_3^- to generate NO_2^-, NH_4^+, and N_2 (Eqs. (4)–(8)). Because $E^\theta(NO_2^-/NH_4^+)$=0.9V, $E^\theta(NO_3^-/NO_2^-)$=0.94V, $E^\theta(NO_3^-/NH_4^+)$=1.2V, $E^\theta(NO_3^-/N_2)$=1.25V, $E^\theta(NO_2^-/N_2)$=1.45V are contained in the energy band of the prepared TiO_2. The holes generated by TiO_2 can react with the hole cleaner HCOOH to generate CO_2^- (Eq. (3)). CO_2^- has a strong reducing ability ($E^\theta(CO_2/CO_2^-)$ =−1.81V), and can directly reduce NO_3^- to N_2 ($E^\theta(NO_3^-/N_2)$=1.25V), NO_2^- ($E^\theta(NO_2^-/N_2)$=1.45V) or NH_4^+ ($E^\theta(NO_3^-/NH_4^+)$=1.2V) (Eqs.(9)–(10)).

$$TiO_2 + hv \rightarrow e^- + h^+ \quad (3)$$

$$HCOO^- + h^+ \rightarrow CO_2 \cdot^- + H^+ \quad (4)$$

$$NO_3^- + 2H^+ + 2e^- \rightarrow NO_2^- + H_2O \quad (5)$$

$$NO_3^- + 10H^+ + 8e^- \rightarrow NH_4^+ + 3H_2O \quad (6)$$

$$2NO_3^- + 12H^+ + 10e^- \rightarrow 2N_2 + 6H_2O \quad (7)$$

$$2NO_2^- + 8H^+ + 6e^- \rightarrow N_2 + 4H_2O \quad (8)$$

$$NO_2^- + 8H^+ + 6e^- \rightarrow NH_4^+ + 2H_2O \quad (9)$$

$$2NO_3^- + 12H^+ + 10CO_2 \cdot^- \rightarrow N_2 + 6H_2O + 10CO_2 \quad (10)$$

$$2NO_2^- + 8H^+ + 6CO_2 \cdot^- \rightarrow N_2 + 4H_2O + 6CO_2 \quad (11)$$

Conclusion

In summary, the layered Ti_3C_2 was successfully prepared by the etching method, and the TiO_2/Ti_3C_2 carrier was prepared by simple calcination, and the effect of calcination temperature on TiO_2/Ti_3C_2 was explored. A chemical reduction method was used to support Ag particles on TiO_2/Ti_3C_2. The effect of silver loading on the performance of photocatalytic nitrate removal was explored. Proposed related mechanisms. Because of the existence of Ti_3C_2 and Ag, the photoinduced electrons quickly migrate to Ti_3C_2 and Ag, thereby promoting the separation of electrons and holes and improved the catalyst activity, so that the removal rate of nitrate reaches 96.1%. Nitrogen selectivity reaches 92.6%. It provides a new method for the removal of nitrate.

Supplementary Information The online version contains supplementary material available at https://doi.org/10.1007/s11356-022-19616-x.

Author contribution Wanying Chen planned and carried out the experimental work. Qingzhao Yao monitored the progress of the experiment and reviewed the draft. Guomeng Dong and Yang Liu contributed to the analysis and interpretation of results. Bo Wu and Changjiang Zuo established and calculated the DFT model; Yiwei Zhang, Yuming Zhou, and Zewu Zhang provided the financial support for the project leading to this publication.

Funding This work was supported by the National Nature Science Foundation of China (21978048), Scientific Innovation Research Foundation of College Graduate in Jiangsu Province (KYCX21_0091), Fundamental Research Funds for the Central Universities (2242015k30001), a Project Funded by the Priority Academic Program Development of Jiangsu Higher Education Institutions (PAPD) (1107047002), and Fund Project for Transformation of Scientific and Technological Achievements of Jiangsu Province of China (BA2019054).

Data availability Not applicable.

Declarations

Ethics approval and consent to participate Not applicable.

Consent for publication Not applicable.

Competing interests The authors declare no competing interests.

References

Baldini E, Palmieri T, Dominguez A, Rubio A, Chergui M (2020) Giant exciton Mott density in anatase TiO_{2}. Phys Rev Lett 125:116403. https://doi.org/10.1103/PhysRevLett.125.116403

Barrabés NSá J (2011) Catalytic nitrate removal from water, past, present and future perspectives. Applied Catalysis B: Environmental 104:1–5. https://doi.org/10.1016/j.apcatb.2011.03.011

Bourkeb K, Wbaaloudj O (2021) Facile electrodeposition of ZnO on graphitic substrate for photocatalytic application: degradation of antibiotics in a continuous stirred-tank reactor. Journal of Solid State Electrochemistry. https://doi.org/10.1007/s10008-021-05045-2

Bredas J, Lhouk KN (2014) DFT elucidation of materials properties. Acc Chem Res 47:3207. https://doi.org/10.1021/ar5003889

Stevens CJ, Gowing DJ (2004) Impact of nitrogen deposition on the species richness of grasslands. SCIENCE 303:1876–1879. https://doi.org/10.1126/science.1094678

Challagulla S, Tarafder K, Ganesan Rroy S (2017) All that glitters is not gold: a probe into photocatalytic nitrate reduction mechanism over noble metal doped and undoped TiO_2. The Journal of Physical Chemistry C 121:27406–27416. https://doi.org/10.1021/acs.jpcc.7b07973

Chen L, Ye X, Chen S, Ma L, Wang Z, Wang Q, Hua N, Xiao X, Cai S, Liu X (2020) Ti_3C_2 MXene nanosheet/TiO_2 composites for

efficient visible light photocatalytic activity. Ceramics International 46:25895–25904. https://doi.org/10.1016/j.ceramint.2020.07.074

Chu S, Wang Y, Guo Y, Feng J, Wang C, Luo W, Fan X, Zou Z (2013) Band structure engineering of carbon nitride: in search of a polymer photocatalyst with high photooxidation property. ACS Catalysis 3:912–919. https://doi.org/10.1021/cs4000624

Fang Y-M, Sun J-J, Wu A-H, Su X-LChen G-N (2008) Catalytic electrogenerated chemiluminescence and nitrate reduction at CdS nanotubes modified glassy carbon electrode. 555-560. https://doi.org/10.1021/la802650e

Feng X, Yu Z, Sun Y, Long R, Shan M, Li X, Liu Y, Liu J (2021) Review MXenes as a new type of nanomaterial for environmental applications in the photocatalytic degradation of water pollutants. Ceramics International 47:7321–7343. https://doi.org/10.1016/j.ceramint.2020.11.151

Fernández-Domene RM, Sánchez-Tovar R, Sánchez-González S, García-Antón J (2016) Photoelectrochemical characterization of anatase-rutile mixed TiO_2 nanosponges. International Journal of Hydrogen Energy 41:18380–18388. https://doi.org/10.1016/j.ijhydene.2016.08.012

Gao J, Jiang B, Ni C, Qi Y, Zhang Y, Oturan N, Oturan MA (2019) Non-precious Co_3O_4-TiO_2/Ti cathode based electrocatalytic nitrate reduction: preparation, performance and mechanism. Applied Catalysis B: Environmental 254:391–402. https://doi.org/10.1016/j.apcatb.2019.05.016

Ghassemi H, Harlow W, Mashtalir O, Beidaghi M, Lukatskaya MR, Gogotsi Y, Taheri ML (2014) In situ environmental transmission electron microscopy study of oxidation of two-dimensional $Ti_3C_2$and formation of carbon-supported TiO_2. Journal of Materials Chemistry A 2. https://doi.org/10.1039/C4TA02583K

Halim J, Cook KM, Naguib M, Eklund P, Gogotsi Y, Rosen J, Barsoum MW (2016) X-ray photoelectron spectroscopy of select multilayered transition metal carbides (MXenes). Applied Surface Science 362:406–417. https://doi.org/10.1016/j.apsusc.2015.11.089

He J, Wu P, Chen L, Li H, Hua M, Lu L, Wei Y, Chao Y, Zhou S, Zhu W, Li H (2021) Dynamically-generated TiO_2 active site on MXene Ti_3C_2: boosting reactive desulfurization. Chemical Engineering Journal 416. https://doi.org/10.1016/j.cej.2021.129022

Hirayama J, Kamiya Y (2014) Combining the photocatalyst Pt/TiO_2 and the nonphotocatalyst SnPd/Al_2O_3 for effective photocatalytic purification of groundwater polluted with nitrate. ACS Catalysis 4:2207–2215. https://doi.org/10.1021/cs5003564

Hong L-f, Guo R-t, Yuan Y, Ji X-y, Li Z-s, W-g L Z-dP (2020) Recent progress of two-dimensional MXenes in photocatalytic applications: a review. Materials Today Energy 18. https://doi.org/10.1016/j.mtener.2020.100521

Hou Z, Chu J, Liu C, Wang J, Li A, Lin T, François-Xavier CP (2021) High efficient photocatalytic reduction of nitrate to N_2 by Core-shell Ag/SiO_2@cTiO_2 with synergistic effect of light scattering and surface plasmon resonance. Chemical Engineering Journal 415. https://doi.org/10.1016/j.cej.2021.128863

Huang K, Li C, Li H, Ren G, Wang L, Wang W, Meng X (2020) Photocatalytic applications of two-dimensional Ti_3C_2 MXenes: a review. ACS Applied Nano Materials 3:9581–9603. https://doi.org/10.1021/acsanm.0c02481

Jia C, Yang P, Li J, Huang B, Matras-Postolek K (2016) Photocatalytic activity evolution of different morphological TiO2 shells on Ag nanowires. ChemCatChem 8:839–847. https://doi.org/10.1002/cctc.201501045

Karen R, Burow BTN, Rupert MG, Dubrovsky NM (2010) Nitrate in groundwater of the United States, 1991−2003. Environ. Sci. Technol. 44:4988–4997. https://doi.org/10.1021/es100546y

Khadidja MF, Fan J, Li S, Li S, Cui K, Wu J, Zeng W, Wei H, Jin H-G, Naik N, Chao Z, Pan D, Guo Z (2021) Hierarchical ZnO/MXene composites and their photocatalytic performances. Colloids and Surfaces A: Physicochemical and Engineering Aspects 628. https://doi.org/10.1016/j.colsurfa.2021.127230

Khan I, Aspalding RF (2004) Enhanced in situ denitrification for a municipal well. Water Res 38:3382–3388. https://doi.org/10.1016/j.watres.2004.04.052

Kim DE, Pak D (2019) Ti plate with TiO_2 nanotube arrays as a novel cathode for nitrate reduction. Chemosphere 228:611–618. https://doi.org/10.1016/j.chemosphere.2019.04.071

Krasae N, Wantala K (2016) Enhanced nitrogen selectivity for nitrate reduction on Cu–nZVI by TiO_2 photocatalysts under UV irradiation. Applied Surface Science 380:309–317. https://doi.org/10.1016/j.apsusc.2015.12.023

Li M, Feng C, Zhang Z, Lei X, Chen R, Yang Y, Sugiura N (2009) Simultaneous reduction of nitrate and oxidation of by-products using electrochemical method. J Hazard Mater 171:724–730. https://doi.org/10.1016/j.jhazmat.2009.06.066

Li ZWY (2019) 2D early transition metal carbides (MXenes) for catalysis. Small 15:e1804736. https://doi.org/10.1002/smll.201804736

Loganathan P, Vigneswaran S, Kandasamy J (2013) Enhanced removal of nitrate from water using surface modification of adsorbents--a review. J Environ Manage 131:363–374. https://doi.org/10.1016/j.jenvman.2013.09.034

Low J, Yu J, Li Q, Cheng B (2014) Enhanced visible-light photocatalytic activity of plasmonic Ag and graphene co-modified Bi_2WO_6 nanosheets. Phys Chem Chem Phys 16:1111–1120. https://doi.org/10.1039/C3CP53820F

Lucchetti R, Onotri L, Clarizia L, Natale FD, Somma ID, Andreozzi R, Marotta R (2017) Removal of nitrate and simultaneous hydrogen generation through photocatalytic reforming of glycerol over "in situ" prepared zero-valent nano copper/P25. Applied Catalysis B: Environmental 202:539–549. https://doi.org/10.1016/j.apcatb.2016.09.043

Mao C-f, X-p Z R-xL (2017) Phenylpropanoic acid-based DESs as efficient extractants and catalysts for the removal of sulfur compounds from oil. Fuel 189:400–407. https://doi.org/10.1016/j.fuel.2016.10.113

Mao C, Yin K, Yang C, Dong G, Tian G, Zhang Y, Zhou Y (2021) Fe-based MOFs@Pd@COFs with spatial confinement effect and electron transfer synergy of highly dispersed Pd nanoparticles for Suzuki-Miyaura coupling reaction. J Colloid Interface Sci 608:809–819. https://doi.org/10.1016/j.jcis.2021.10.055

Meng Q, Ma J, Zhang Y, Li Z, Zhi C, Hu A, Fan J (2018) The S-functionalized Ti_3C_2 Mxene as a high capacity electrode material for Na-ion batteries: a DFT study. Nanoscale 10:3385–3392. https://doi.org/10.1039/C7NR07649E

Meng X, Zhang G, Li N (2017) Bi24Ga2O39 for visible light photocatalytic reduction of Cr(VI): controlled synthesis, facet-dependent activity and DFT study. Chemical Engineering Journal 314:249–256. https://doi.org/10.1016/j.cej.2016.12.090

Naguib M, Kurtoglu M, Presser V, Lu J, Niu J, Heon M, Hultman L, Gogotsi Y, Barsoum MW (2011) Two-dimensional nanocrystals produced by exfoliation of Ti_3AlC_2. Adv Mater 23:4248–4253. https://doi.org/10.1002/adma.201102306

Naguib M, Mochalin VN, Barsoum MW, Gogotsi Y (2014) 25th anniversary article: MXenes: a new family of two-dimensional materials. Adv Mater 26:992–1005. https://doi.org/10.1002/adma.201304138

Nila A, Baibarac M, Udrescu A, Smaranda I, Mateescu A, Mateescu G, Mereuta P, Negrila CC (2019) Photoluminescence and structural properties of the nitrogen doped TiO_2 and the influence of SiO_2 and Ag nanoparticles. J Phys Condens Matter 31:375201. https://doi.org/10.1088/1361-648X/ab2692

Quyen VT, Ha LTT, Thanh DM, Le QV, Viet NM, Nham NT, Thang PQ (2021) Advanced synthesis of MXene-derived nanoflower-shaped TiO_2@Ti_3C_2 heterojunction to enhance photocatalytic

degradation of rhodamine B. Environmental Technology & Innovation 21. https://doi.org/10.1016/j.eti.2020.101286

Rathinavelu JR, Jung M-J, Im J-S, Seak-Lee Y, Palanivelu K (2013) Electrospinning of polymer-unaided TiO_2 fibers and iron impregnation for sunlight-induced photo-Fenton's degradation of dyes. Environmental Engineering Science 30:653–662. https://doi.org/10.1089/ees.2012.0051

Shah SA, Habib T, Gao H, Gao P, Sun W, Green MJ, Radovic M (2016) Template-free 3D titanium carbide ($Ti_3C_2T_x$) MXene particles crumpled by capillary forces. Chem Commun (Camb) 53:400–403. https://doi.org/10.1039/C6CC07733A

Shi H, Zhang T, Wang H, Wang X, He M (2011) Photocatalytic conversion of naphthalene to α-naphthol using nanometer-sized TiO_2. Chinese Journal of Catalysis 32:46–50. https://doi.org/10.1016/S1872-2067(10)60158-1

Sittinun Tawkaew YF, Yin S, Sato T (2001) Synthesis of cadmium sulfide pillared layered compounds and photocatalytic reduction of nitrate under visible light irradiation. Colloids and Surfaces A Physicochemical and Engineering Aspects 179:139–144. https://doi.org/10.1016/S0927-7757(00)00649-X

Sivakumar S, Selvaraj A, Ramasamy AK, Balasubramanian V (2013) Enhanced photocatalytic degradation of reactive dyes over $FeTiO_3/TiO_2$ heterojunction in the presence of H_2O_2. Water, Air, & Soil Pollution 224. https://doi.org/10.1007/s11270-013-1529-x

Soares OSGP, Pereira MFR, Órfão JJM, Faria JL, Silva CG (2014) Photocatalytic nitrate reduction over Pd–Cu/TiO_2. Chemical Engineering Journal 251:123–130. https://doi.org/10.1016/j.cej.2014.04.030

Sreedhar ANoh J-S (2021) Recent advances in partially and completely derived 2D Ti_3C_2 MXene based TiO_2 nanocomposites towards photocatalytic applications: a review. Solar Energy 222:48–73. https://doi.org/10.1016/j.solener.2021.05.010

Tian F, Zhu R, Song K, Ouyang F, Cao G (2015) The effects of amount of La on the photocatalytic performance of $ZnIn_2S_4$ for hydrogen generation under visible light. International Journal of Hydrogen Energy 40:2141–2148. https://doi.org/10.1016/j.ijhydene.2014.12.025

Wu G, Katsumura Y, Muroya Y, Lin M, Morioka T (2002) Temperature dependence of carbonate radical in $NaHCO_3$ and Na_2CO_3 solutions: is the radical a single anion. J. Phys. Chem 106,:2430-2437. https://doi.org/10.1021/jp013401p

Xiong Z, Lei Z, Li Y, Dong L, Zhao Y, Zhang J (2018) A review on modification of facet-engineered TiO_2 for photocatalytic CO_2 reduction. Journal of Photochemistry and Photobiology C: Photochemistry Reviews 36:24–47. https://doi.org/10.1016/j.jphotochemrev.2018.07.002

Yu B, Tawiah B, Wang LQ, Yin Yuen AC, Zhang ZC, Shen LL, Lin B, Fei B, Yang W, Li A, Zhu SE, Hu EZ, Lu HD, Yeoh GH (2019) Interface decoration of exfoliated MXene ultra-thin nanosheets for fire and smoke suppressions of thermoplastic polyurethane elastomer. J Hazard Mater 374:110–119. https://doi.org/10.1016/j.jhazmat.2019.04.026

Zhang D, Qiu R, Song L, Eric B, Mo Y, Huang X (2009) Role of oxygen active species in the photocatalytic degradation of phenol using polymer sensitized TiO_2 under visible light irradiation. J Hazard Mater 163:843–847. https://doi.org/10.1016/j.jhazmat.2008.07.036

Zhang F, Chen J, Zhang X, Gao W, Jin R, Guan N (2004a) Simple and low-cost preparation method for highly dispersed Pd/TiO_2 catalysts. Catalysis Today 93-95:645–650. https://doi.org/10.1021/cm034306r

Zhang F, Chen J, Zhang X, Gao W, Jin R, Li N, Ga Y (2004b) Synthesis of titania-supported platinum catalyst: the effect of pH on morphology control and valence state during photodeposition. Langmuir 20:9329–9334. https://doi.org/10.1021/la049394o

Zhang F, Guan N, Li Y, Zhang X, Chen J, Zeng H (2003) Control of morphology of silver clusters coated on titanium dioxide during photocatalysis. 19:8230–8234. https://doi.org/10.1021/la034917y

Zhang H, Liu Z, Li Y, Zhang C, Wang Y, Zhang W, Wang L, Niu L, Wang P, Wang C (2020a) Intimately coupled TiO_2/g-C_3N_4 photocatalysts and in-situ cultivated biofilms enhanced nitrate reduction in water. Applied Surface Science 503. https://doi.org/10.1016/j.apsusc.2019.144092

Zhang L, Peng C-T, Shi JLR (2020b) Surface alloying of chromium/tungsten/stannum on pure nickel and theoretical analysis of strengthening mechanism. Applied Surface Science 532. https://doi.org/10.1016/j.apsusc.2020.147477

Zhang Y, Kirk C, Robertson N (2020c) Nitrogen doping and carbon coating affects substrate selectivity of TiO_2 photocatalytic organic pollutant degradation. Chemphyschem 21:2643–2650. https://doi.org/10.1002/cphc.202000492

Zhao B, Li X, Wang Y, Tan X, Qi W, Li H, Wei J, You Y, Shi W, Zhang Q (2021) Dissimilatory nitrate reduction and functional genes in two subtropical rivers. Environ Sci Pollut Res Int, China. https://doi.org/10.1007/s11356-021-15197-3

Zhao MQ, Xie X, Ren CE, Makaryan T, Anasori B, Wang G, Gogotsi Y (2017) Hollow MXene spheres and 3D macroporous MXene frameworks for Na-Ion storage. Adv Mater 29. https://doi.org/10.1002/adma.201702410

Zhao Y, Que M, Chen J, Yang C (2020) MXenes as co-catalysts for the solar-driven photocatalytic reduction of CO_2. Journal of Materials Chemistry C 8:16258–16281. https://doi.org/10.1039/D0TC02979C

Zhu N, Wu Y, Tang J, Duan P, Yao L, Rene ER, Wong PK, An T, Dionysiou DD (2018) A new concept of promoting nitrate reduction in surface waters: simultaneous supplement of denitrifiers, electron donor pool, and electron mediators. Environ Sci Technol 52:8617–8626. https://doi.org/10.1021/acs.est.8b01605